



Budapest University of Technology and Economics
Faculty of Mechanical Engineering
Department of Hydrodynamic Systems

Modelling approaches in aneurysm-related flow simulations

Booklet of PhD Dissertation

Written by: Dániel Gyürki
mechanical modelling engineer

Supervisor: Dr. György Paál
professor

Budapest, 2024. 05. 31.

1 Introduction

The vessels of the cardiovascular system are prone to different vessel wall malformations when the shape, structure or integrity of the vessel wall is impaired. Each malformation results in different blood flow patterns, deviating from physiologically healthy conditions. The main topic of this dissertation is related to one of these malformations, namely aneurysms. One type, the saccular aneurysm, is a berry-like asymmetric bulging of the vessel wall (see Figure 1). These are found dominantly on the arteries of the brain, mainly around the segments of the Circle of Willis (CoW).

Initiation of intracranial aneurysms (IA) is a widely researched topic. The initiation process is an inflammatory response of the vessel wall. The wall shear stress (WSS) resulting from unsteady, oscillatory blood flow in complex geometries or simply the elevated WSS of an impinging jet causes endothelial dysfunction, which results in a cascade process of revascularization. This revascularization is the cradle of aneurysm initiation. The growth phase can end in three different scenarios. The aneurysm either stabilizes and does not grow further or ruptures from the continuous weakening of the wall and the pressure loads, or the aneurysm is treated to remove the risk of rupture. There are multiple methods to treat an aneurysm. This dissertation deals with flow diverter (FD) stents, which are usually weaved from thin wires. The FDs reside inside the catheter. After reaching the aneurysm, the FD is pushed out of the catheter, and it expands and slides onto the wall. The flow inside the sac slows down as the FD acts as a hydrodynamic resistance.



Figure 1: Intracranial aneurysm (IA) found after the carotid syphon, near the Circle of Willis.

Initiation, growth and rupture of the described vessel wall malformation are significantly influenced by the blood flow in the specific region. Therefore, it is important to thoroughly investigate the local and global flow conditions in the arterial system. There are multiple ways to study blood flow. The most common way is to measure the desired quantities, which are the pressure and velocity or volumetric flow rate. The other significant part

of the engineering community models the cardiovascular system on the computer. These computer models can be either global, taking into consideration the whole arterial system or even the whole cardiovascular system, or can focus on local problems. Usually, 1D models are used for global problems, and localized research uses 2D or 3D computational models.

First, computational fluid dynamic (CFD) simulations were one-dimensional, as the governing equations are easier to solve with limited computational power. 1D simulations deal mainly with the global arterial system. One of the first works was made by Avolio [1], who used the impedance model to simulate the blood flow in an arterial graph with 128 vessels. The big advantage of 1D CFD is the ability to combine with other higher or lower-dimensional models. Three-dimensional flow simulations are widely used nowadays in the topic of hemodynamics, as the CFD solvers are widely available, and the medical imaging techniques (Computed Tomography Angiography - CTA, Magnetic Resonance Angiography - MRA, Digital Subtraction Angiography - DSA) can provide accurate geometries. One of the advantages of 3D CFD is that it can produce quantities that are hard to measure, for example, wall shear stresses. In the topic of IAs, CFD simulations can be found in initiation [2], [3], growth and rupture [4], [5], and treatment [6], [7] researches. The topic of intracranial aneurysms is well summarized in Fukuda et al. [8].

This dissertation can be considered as the continuation of the history of hemodynamics-related research at the Department of Hydrodynamic Systems. The main aim of the dissertation is to present different modelling approaches related to hemodynamic simulations, namely:

1. Creation of a patient-specific one-dimensional model of the arterial system which can be used for estimating central arterial pressure or for providing boundary conditions for 3D simulations.
2. Investigation of the paths of massless, passive particles, in order to qualitatively and quantitatively describe the chaotic nature and the mixing effect of the flow on the particle paths.
3. Quantitative comparison of the hydrodynamic resistance of flow diverters from different manufacturers in different deployment scenarios, which can further be used in CFD simulations of FD treatments.

2 Patient-specific modelling of the arterial system

2.1 Introduction

Aortic blood pressure is an essential indicator of an individual's circulatory status in health assessment. The blood pressure varies along the arterial system both in the mean and shape of the curve, but aortic (central) blood pressure has a distinguished role. For example, aortic pressure and the metric derived from it can serve as a guideline in the case of healthy patients [9] or in the case of cardiovascular events [10].

Estimating the aortic pressure based on the radial or the brachial pressure is of great importance. Papaioannou et al. [11] provided a comprehensive summary about central blood pressure estimation. One-dimensional CFD simulations are also applicable for central pressure estimation, as well as providing other physiological parameters.

This section presents a reduction method for the number of patient-specific parameters with a novel so-called backward calculation method (backward from the peripheries towards the heart). Then, an optimization procedure is presented first to prove the reduction method and the patient-specificity, then later to determine those parameters. The aim of these patient-specific 1D arterial models is to estimate the central pressure based on peripheral pressure measurements. The model can also present patient-specific boundary conditions for 3D CFD simulations if needed.

2.2 Methods

The one-dimensional model used in this dissertation is the same one as that developed by Gergely Bárdossy, described in his articles [12] and [13].

The flow in the arterial system is time-dependent, but quasiperiodic, based on the beating of the heart. The 1D governing equations (the continuity equation and the momentum equation) are supplemented with the equations of the Poynting-Thomson model, which takes into account the viscoelastic behaviour of the vessel wall. The Method of Characteristics (MoC) can be applied to solve the final equation system. Instead of the traditional forward calculation method (where the characteristic lines march forward in time), a so-called backward calculation method is used, which is introduced by Bárdossy and Halász [13]. In the proposed method, if the velocity and pressure are both known at the end of a segment for all time instances, then the characteristic lines can march backwards in space, in contrast with the forward in time marching. This method can be used to estimate the central pressure based on peripheral pressure measurement.

Next, a graph of the arterial system is needed. Only the major vessels of the arterial tree are considered, while the neglected vessels and the venous system are modelled by boundary conditions. In total, there are 50 branches, 24 inner nodes, which connect the segments, and 28 peripheral nodes. Each branch segment has six parameters (the length, the diameter, the vessel wall thickness and the three material parameters of the vessel wall), while the nodes have one parameter (ohmic resistance). Altogether, there are 352 parameters (300 branch and 52 nodal). Finding a patient-specific value for this huge amount of parameters is a difficult task. Therefore, simplifications are needed.

The first reduction is about the lengths of the branches. The original length values are multiplied by the height ratio of the current patient and Avolio's patient [1]. The viscous material property was fine-tuned by Bárdossy and Halász [12]. With this, the lengths and the wall viscosity were excluded from the optimization procedure. The vessel wall thickness is considered as the tenth of the vessel diameter. A further parameter reduction is based on the fact that a particular branch/node parameter does not change independently in different parts of the body but rather scales uniformly in the whole system. The diameters of the branches and the ohmic resistances at the nodes are modified according to this rule. For the remaining material parameters, an assumption was made about the wave speed. Based on the data of [14], the wave speed increases parabolically from the heart towards the peripheries as the function of the distance from the heart, normalized with the maximum distance at a given path. The remaining parameter is the other elastic modulus of the Poynting-Thomson model, which is considered with a proportionality constant referenced to the main elastic modulus.

With the help of these assumptions, the number of the patient-specific parameters are reduced from 352 to 5, which are the following:

- α_D : proportionality parameter of the diameters
- α_ζ : proportionality parameter of the resistances
- α_E : ratio of the elastic moduli
- α_0 : constant coefficient of the parabolic wave speed curve
- α_A : quadratic coefficient of the parabolic wave speed curve

The first part of the research concentrated on whether the arterial graph with these five parameters can accurately reproduce the central pressure curve. Therefore, an optimum set of these parameters were obtained by minimizing the difference between a measured aortic pressure curve and a backward calculated one using radial pressure is measurement. In the second part, two peripheral pressure signals were measured (at the carotid and at the radial artery) and the difference between the two backward calculated aortic pressure curves was the basis of the optimization.

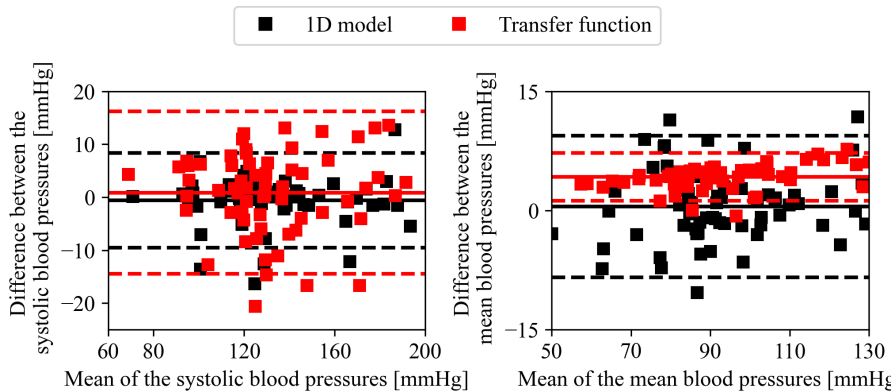


Figure 2: Bland-Altman plots for the Systolic Blood Pressure (SBP) (left) and the Mean Blood Pressure (MBP) (right). Black is the comparison of the two backward calculated curves, while red is the comparison of the backward calculated and the transfer function methods. The solid line is the mean of the values, the dashed lines represents the ± 1.96 Standard Deviation (SD).

2.3 Results

Despite the drastic reduction on the number of parameters, a very good agreement was achieved with the catheter-based aortic pressure measurement. Altogether, based on 22 patients' data, my method overestimated the systolic blood pressure (SBP) and mean blood pressure (MBP) on average by 0.6 and 0.5 mmHg with standard deviation (SD) of 3.1 and 0.5 mmHg, respectively. The average root mean square difference (RMSD) between the measured and the calculated pressure curves was 3 mmHg with SD of 1.2 mmHg.

After I was convinced that despite the drastic simplification, this arterial model with only five patient-specific parameters can approximate the central pressure curve, the next method was tested. Bland-Altman plots were generated for 62 patients whose patient-specific parameters were obtained using two peripheral pressure measurements. This time, my method is compared with the widely popular transfer function method [15]. Based on Figure 2, the Bland-Altman plots show good agreement between the two backward-calculated aortic pressure curves. The estimation of SBP and MBP from the two curves differs on average by 0.5 and -0.5 mmHg with SD of 4.6 and 4.6 mmHg, respectively. The average RMSD between the two calculated curves was 5.9 mmHg with SD of 3.5 mmHg. These values show that for general clinical applications, this method is an effective way to get patient-specific arterial graph parameters, as well as a central pressure curve.

The average difference in the SBP-s between the backward calculation and the transfer function methods is 0.9 mmHg with SD of 7.9 mmHg, while the MBP of the backward calculated pressure curve is larger on average 4.2 mmHg with SD of 1.5 mmHg. Therefore, a good agreement exists between the two methods. Particularly, the transfer function method underestimates the backward calculation method. However, the SD of the difference between the two methods regarding the MDP is generally small.

According to the results of this section, it can be said that despite the great parameter reduction, the arterial model can accurately reproduce the patient-specific central pressure curve. Furthermore, a method is provided in order to acquire the patient-specific set of the parameters based on two peripheral pressure measurements. The patient-specific 1D arterial graph can be used for producing boundary conditions for local 3D simulations.

Contribution 1

The several hundred parameters of the simplified numerical model of an arterial graph described in Bárdossy and Halász [13] can be reduced to five parameters. These parameters are the following:

- $\alpha_D = \frac{D_i}{D_{ref,i}}$: proportionality parameter of the diameters
 - $\alpha_\zeta = \frac{\zeta_i}{\zeta_{ref,i}}$: proportionality parameter of the resistances
 - $\alpha_E = \frac{E_1}{E_2}$: ratio of the elastic moduli
 - α_0 : constant coefficient of the wave speed curve
 - α_A : quadratic coefficient of the wave speed curve
- $$a_i = \alpha_0 + \alpha_A \left(\frac{L_i}{L_{max}} \right)^2$$
- $$a_i = \alpha_0 + \alpha_A \left(\frac{L_i}{L_{max}} \right)^2$$

where D_i is the diameter of the i -th branch, $D_{ref,i}$ is the reference value from the literature for the diameter, ζ_i is the resistance of the i -th node, $\zeta_{ref,i}$ is the reference value from the literature for the resistance, a_i is the wave speed of the i -th branch, L_i is the distance of the proximal end of the i -th segment measured from the heart, L_{max} is the maximum distance along the path in question, and E_1 and E_2 are the elastic moduli of the Poynting-Thomson model.

The numerical model of the arterial graph using these five parameters can accurately reproduce the patient-specific aortic pressure curve according to the following calculation steps:

1. Measure the peripheral pressure signal at the radial artery and the pressure signal in the aorta.
2. Calculate the aortic pressure curve from the peripheral point using the backward-calculation method described in Bárdossy and Halász [13].
3. Calculate the objective function by the weighted sum of H_1 and H_2 :

$$H_1 = \sqrt{\frac{1}{T} \int_0^T (p_{meas}(t) - p_{calc}(t))^2 dt} \quad (1)$$

$$H_2 = \sqrt{\frac{1}{T - T_{dia}} \int_{T_{dia}}^T v^2(t) dt} \quad (2)$$

where T is the period time of the heart cycle, T_{dia} is the start of the diastolic phase, $p_{meas}(t)$ and $p_{calc}(t)$ are the measured and backward calculated aortic pressure curves, respectively, and $v(t)$ is the aortic velocity curve. The weights of H_1 and H_2 are 3 and 1, respectively.

4. Use a minimum searching algorithm (e.g., Nelder-Mead algorithm) and tune the parameters of the arterial graph in order to minimize the objective function.

Related publications: [J1] and [J2].

Contribution 2

Patient-specific aortic pressure can be calculated based on two peripheral pressure measurement signals. The calculation should follow the following steps:

1. Measure two peripheral pressure signals (e.g., carotid and radial arteries).
2. Calculate the aortic pressure curves from each point using the backward-calculation method described in Bárdossy and Halász ([13]).
3. Calculate the objective function by the weighted sum of H_1 and H_2 :

$$H_1 = \sqrt{\frac{1}{T} \int_0^T (p_1(t) - p_2(t))^2 dt} \quad (3)$$

$$H_2 = \sqrt{\frac{1}{T - T_{dia}} \int_{T_{dia}}^T v^2(t) dt} \quad (4)$$

where T is the period time of the heart cycle, T_{dia} is the start of the diastolic phase, $p_1(t)$ and $p_2(t)$ are the aortic pressure curves calculated from the two pressure measurements, respectively, and $v(t)$ is the aortic velocity curve. The weights of H_1 and H_2 are 3 and 1, respectively.

4. Use a minimum searching algorithm (e.g., Nelder-Mead algorithm) and tune the parameters of the arterial graph in order to minimize the objective function.

Related publications: [J1] and [J2].

3 Modelling particle paths

3.1 Introduction

One technique in vessel wall malformation research can be the usage of fictive particles or ink, which are released in the flow domain, and their paths or concentration is calculated. One of two approaches in residence time or particle tracking metrics is the Lagrangian method, where the usually massless particles are propagated by the flow inside the domain, and the particle residence time (PRT) is calculated.

Calculating particle paths can also model other vital aspects of human physiology, for example, thrombus deposition in geometries [16] or particles travelling with the blood flow during drug administration [17]. However, it is important to note that Závodszy et al. [18] found that particles show chaotic nature when placed inside perianeurysmal flow. One reason behind this phenomenon may be the fact that even though the flow is laminar in the cerebral arteries in most cases, instabilities may arise during certain parts of the cardiac cycle, dominantly in the decelerating phase [19].

In this section, the particle paths are calculated in patient-specific geometries. The first aim is a dependence study, where the effect of the refinement of the voxel size and integrator time step size is investigated on the particle paths. Then, the effect of the presence of the aneurysm sac and the particle release time is observed on the particle paths. The effect of the sac is investigated by virtually removing the aneurysm to have a geometry which is similar to the one before the aneurysm initiation.

3.2 Methods

The procedure starts with obtaining the geometry and preparing it for the simulations. In order to assess the effect of the aneurysm sac on the particle paths, a virtually reconstructed version is also prepared. Next step is the creation of a voxel field for the numerical simulation.

After the voxel field is generated, a numerical flow simulation is performed using the lattice-Boltzmann method. A parabolic velocity boundary condition is prescribed at the inlet of the domain. A signal modulates the maximum of the parabola. At the peak of the cycle, the Reynolds number, based on the cross-sectional average velocity at the inlet is chosen to be 250 for every case. The smallest outlet is prescribed as a static pressure outlet with 0 Pa. The other outlets are velocity outlets with parabolic velocity profiles. The velocities at each outlet are calculated based on Murray's law, which divides the volumetric flow rates proportionally to the second power of the areas of the outlets. Lastly, the bounce-back scheme is prescribed at the voxels assigned with the wall flag during voxelization. The flow simulations were transient (time-dependent), and the time step was determined according to the stability criterion of the LBM and depended on the voxel size. The time step was around 10^{-5} seconds, and the velocity field was saved at every 0.01 second. The simulations were performed using an in-house code, written in C++, based on the open-source code package Palabos [20].

After obtaining the velocity fields, the next step is calculating the paths of one million massless, passive particles placed in the flow field. As for now, the particles do not represent any physiological processes, but in the future, it is possible to modify this method in order to represent targeted drug delivery or thrombus formation. The velocity field has to be integrated along the particle path from a starting position to acquire the positions of a given particle at a given time. The integrations were performed using a fourth-order Runge-Kutta method with a fixed time step. The integrator is an in-house code written in C++. The integration is done for 10 seconds (10 heart cycles) to allow enough time for the particles to leave the observed domain. Each particle is labelled by two outputs: a particle residence time (PRT) and an outlet.

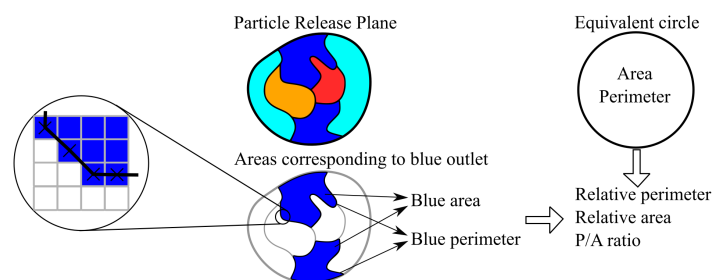


Figure 3: Schematic figure of the relative perimeter, relative area and their ratio calculation.

In order to compare different scenarios, the outlets are further processed. The particle release plane is colored according to the outlet through which the particle starting from that point leaves the domain. Then, the next step is to summarize the perimeter and area of the regions corresponding to one outlet. These sums are normalized with the perimeter and area of an area-equivalent circle to the cross-section of the releasing plane. Obviously, the area corresponding to each outlet is always finite. However, if the resulting particle paths display increasingly chaotic nature, they show a filamentary structure when projected onto the particle release plane, so the respective perimeter grows. Therefore, the perimeter-to-area ratio (P/A ratio) for a given outlet will grow as the particle paths become more folded. The method is shown schematically in Figure 3.

After an initial investigation of the voxel size and integrator time step dependence based on results from five aneurysms, the main research took place, where the effect of the aneurysm sac and the particle release time is investigated in 26 geometries with real life aneurysms.

3.3 Results

Ten calculations were performed for each case and each version (with or without aneurysm) with different particle release times. Every simulation setting is the same, only the presence of the aneurysm sac or the particle release time is different. The results can be seen in Figure 4 for one geometry with the aneurysm sac still on. Similar figures could be made for the other cases and versions as well.

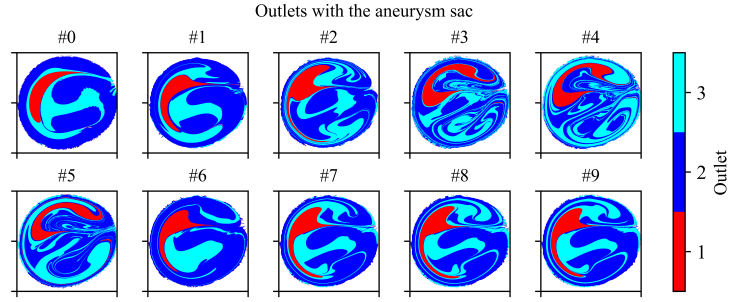


Figure 4: The results of the different particle release times for Case3. The inlet plane is colored according to the outlets through which the particles leave the domain.

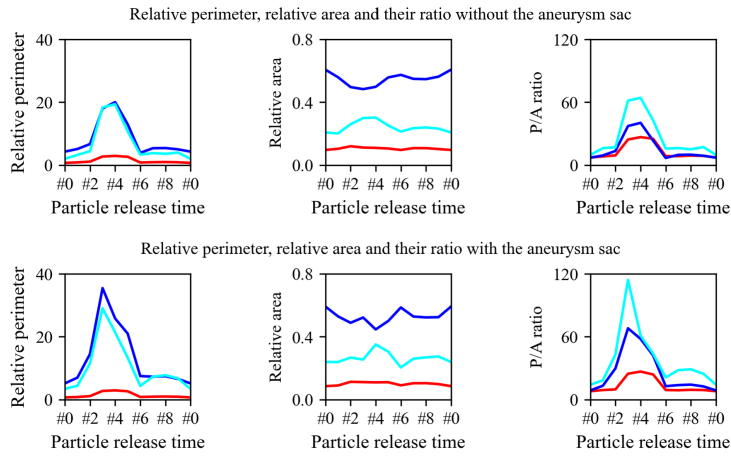


Figure 5: Relative perimeter, relative area and their of each outlet for Case3 without (top) and with aneurysm (bottom) as the function of particle release time.

It can be easily seen in Figure 4 that the areas corresponding to different outlets display drastically different natures in the different subplots. While the results of the release at the instant #0 show easily distinguishable, simple areas between the three outlets, the plots corresponding to other release times during the heart cycle display a more complex, filamentary structure (e.g. #3, #4 and #5). The simpler, well-defined areas resume if the particles are released later in the heart cycle (e.g. #7, #8 and #9). The aforementioned relative perimeter, relative area and their ratio are calculated for each particle release time and the version without the aneurysm sac as well. These can be seen in Figure 5. The top row is without the aneurysm, while the bottom row is the version with the aneurysm. The different particle release times are on the horizontal axes.

Similar figures can be presented for the other cases as well. Based on the numerical results (the P/A ratios), ANOVA was performed in order to assess the effect of the aneurysm sac presence and the particle release time through the heart cycle. According to the ANOVA performed on 26 real aneurysm geometries, the particle release time and the presence of the aneurysm sac both have significant effect ($p < 5.71e-35$ and $9.36e-12$, respectively) on the P/A ratio. The results show, that the P/A ratio increases when the particles are still inside the domain during the decelerating phase of the heart cycle, and the ratio decreases otherwise. Similarly, the aneurysm sac increases the P/A ratio compared to the virtually reconstructed version.

The results of this section provides a greater understanding in the paths of small, massless, passive particles placed inside the flow field of aneurysm geometries. As for now, the particles are not part of any physiological processes. However, in the future, the particles can be considered as part of blood coagulation (platelet activation) or targeted drug use (microparticles carrying drugs).

Contribution 3

The massless, passive virtual particles display chaotic nature when released inside the flow field of an aneurysm. The chaotic nature of these particles released inside the flow of the aneurysm is investigated by the following calculation and evaluation protocol:

1. Acquire the time-dependent velocity field of the flow inside an aneurysm.
2. Calculate the paths of passive, massless virtual particles by integrating the velocity field, starting from the points of the release plane. Register the outlet through which the particle leave the observed domain.
3. Find the regions on the release plane corresponding to each outlet. Summarize the areas and perimeters of regions, corresponding to the outlets separately, and normalize them with the area and perimeter of a circle with equivalent area of the releasing cross-section.
4. Calculate the perimeter over the area ratio of the normalized values (P/A ratio).

The P/A ratio is large if the regions display a folded, filamentary nature, since the normalized area is bounded and cannot be larger than one, while the perimeter has no upper limit.

Based on the ANOVA performed on 26 real aneurysm geometries, the particle release time and the presence of an aneurysm sac have significant ($p < 5.71e-35$ and $p < 9.36e-12$, respectively) effect of the P/A ratio. According to the results of the 26 geometries, the P/A ratio is increased, when the particles are still inside the domain during the decelerating phase of the heart cycle, and the P/A ratio decreases otherwise.

Related publications: [J3], [J4], [C1] and [C2].

4 Stent resistance measurements

4.1 Introduction

Flow diverter stent implantation is an effective technique for the treatment of large and broad-necked sidewall aneurysms [21]. Despite the high efficacy of flow diversion [22], some aneurysms still fail to occlude following the FD treatment. The efficacy of flow diversion is determined by the geometric parameters of the device and the deployment technique used by the operator, for example more/less forward pushing [23], or radial sizing [24]. These factors have an impact on the effective flow reducing capacity of the FD, also called the hydrodynamic resistance (HR).

In vitro measurements and computational fluid dynamics investigating the flow patterns in the aneurysm sac have been used to quantify the efficacy of FDs [7]. If no detailed flow structures are needed around the individual struts, then the FD can be simulated as a homogeneous porous layer covering the target vessel [25]. However, such simulations necessitate accurate knowledge of the HR of the porous layer [26].

The purpose of this research is to determine the flow reduction capacity of FD stents from various manufacturers, expressed as the HR. The HR is determined, using different deployment techniques and sizing strategies and correlated with geometric parameters of the devices. These measurements aim at providing data for porous media-based CFD simulations, assisting neurointerventionalists in choosing the appropriate device and technique, based on quantitative results.

4.2 Methods

Every solid object placed in a flow presents a hydrodynamic resistance manifested in a pressure loss (Equation 5).

$$\Delta p = aQ^2 + bQ \tag{5}$$

where Δp is the measured pressure drop, Q is the volumetric flow rate, a is the quadratic coefficient and b is the linear coefficient.

An experimental rig (see left side of Figure 6) was developed to model the flow through the FD stents for the measurements. The main idea of the setup is to place the stent into tailor-made holder tubes and measure the resistance of the mesh. The FDs were implanted into the holder tube by a skilled neurointerventionalist. Two different FD designs were used from two manufacturers (Pipeline Embolization Device, Medtronic plc, Minneapolis, MN, USA: referred to as PED; P64 flow modulation device, Phenox Inc., Bochum, Germany: referred as P64). FDs of 5, 4 and 3 mm diameters by both manufacturers were measured, referred later as FD5, FD4 and FD3, respectively. The holder tubes also have these three different diameters, referred later as Tube5, Tube4 and Tube3, respectively. Different FDs were deployed into the same-sized holder tube using different techniques in terms of

longitudinal device compression or elongation. To test the effect of radial sizing, first, we performed measurements with the nominal diameter of the stents matching the diameter of the holder tube (e.g. FD5 in Tube5). These scenarios are called nominal sizing. The effects of oversizing were tested by placing the FD in a 1 mm smaller diameter tube, than its nominal diameter (e.g. FD5 in Tube4).

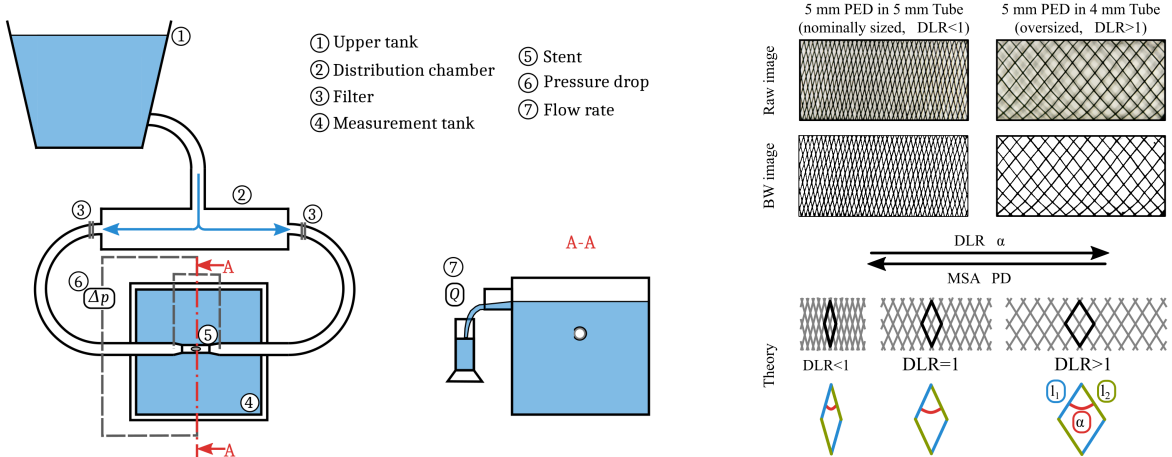


Figure 6: Left: Sketch of the final measurement rig. Right: Evaluation procedure of the images and the sketch of the DLR, PD, MSA relation.

A strict measurement protocol was developed, based on previous experiences in order to ensure reproducibility and consistency. After the implantation, the protocol starts with a microscopic photograph of the implanted device at the elliptical hole with a USB microscope for further image processing. The deployed length of the device (L_2) is also recorded. The next step is the HR measurement. Each FD deployment was measured four times (each times with at least 10 measurement points) to estimate the measurement uncertainties. During the HR measurements, the temperature of the water is also recorded. The density of the water changes only a little as the function of the temperature, but the viscosity depends sensitively on it. After the fourth time, the devices were taken out of the holder tube. The unconstrained length and diameter were recorded, and a microscopic photograph was taken. The empty holder tube was put inside the measurement rig. The HR curves of the empty holder tubes were measured four times as well, in order to quantify the system resistance.

The evaluation starts with the processing of the images (see right side of Figure 6). A central rectangular cutout of the stent was selected in order to avoid the distortion caused by the cylindrical shape. Then a black and white image was created from the cropped image. The geometrical data were obtained from this black and white image. The ratio of the area covered by the struts and the whole area is calculated, which is the so-called metallic surface area (MSA). Then, the pore density (PD) is measured by counting the number of pores and dividing it with the area. The next step in the procedure is the evaluation of the measured HR curves, which were performed with water at different

temperatures. The main step is to transform coefficients of the HR curve measured with water to 37 °C blood. This is necessary if the values are used in CFD simulations because the material properties of the fluid in these simulations are of blood. The transformation is performed by nondimensionalizing the HR equation by introducing the nondimensional pressure number and the Reynolds number.

Altogether, after the evaluation procedure, the following data are acquired for every deployment scenario: quadratic coefficient of the hydrodynamic resistance curve (a_b), linear coefficient of the hydrodynamic resistance curve (b_b), deployment length ratio (DLR), metallic surface area (MSA) and pore density (PD).

4.3 Results

First, the difference between a nominally sized and an oversized FD for a given holder tube, thus the effect of device sizing is investigated. Figure 7 demonstrates these results for Tube4 and Tube3 at a fictive pressure drop calculated with $Q = 5$ ml/s. Next, I observed the effect of the deployment technique, namely the longitudinal compression or elongation during deployment (see Figure 8). Lastly, the effect of the strut number (different manufacturer) is investigated.

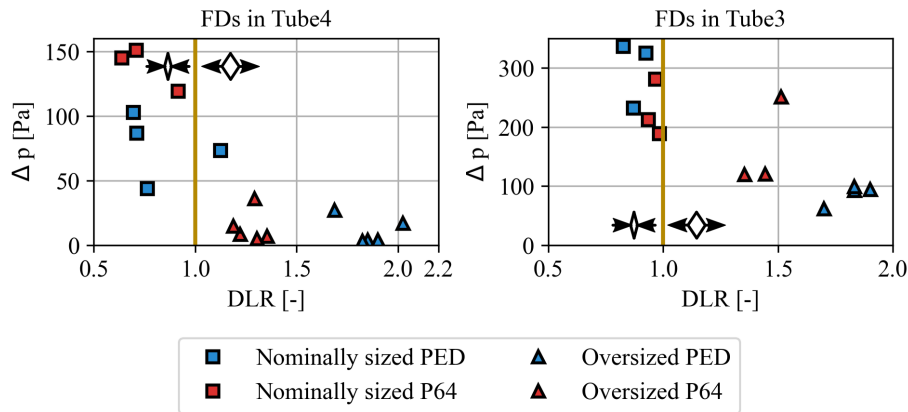


Figure 7: The effects of radial sizing in the case of FD5 and FD4 in Tube4 (left), and FD4 and FD3 in Tube3 (right) measurements, pressure drop calculated with 5 ml/s flow rate as the function of the deployment length ratio. The vertical yellow lines represent the nominal deployment length, the small pictograms represent the longitudinally compressed and elongated deployment scenarios. Blue markers correspond to PED, while red markers correspond to P64 measurements. Squares are the nominally sized and triangles are the oversized cases.

It is visible that the pressure drop makes a noticeable jump between the oversizing and the nominal sizing. The results suggest that choosing an oversized stent for treating an aneurysm over a nominally sized stent may produce insufficient resistance through the aneurysm neck. Therefore, the thrombosis in the sac may not be complete. Similarly, both MSA and PD depend on the deployment length, hence the longitudinal compression/elongation. This phenomenon is closely related to the change in HR. Lastly, the structural difference between the two manufacturers is the number of struts, which unequivocally determines the MSA and PD values because of the braided geometry.

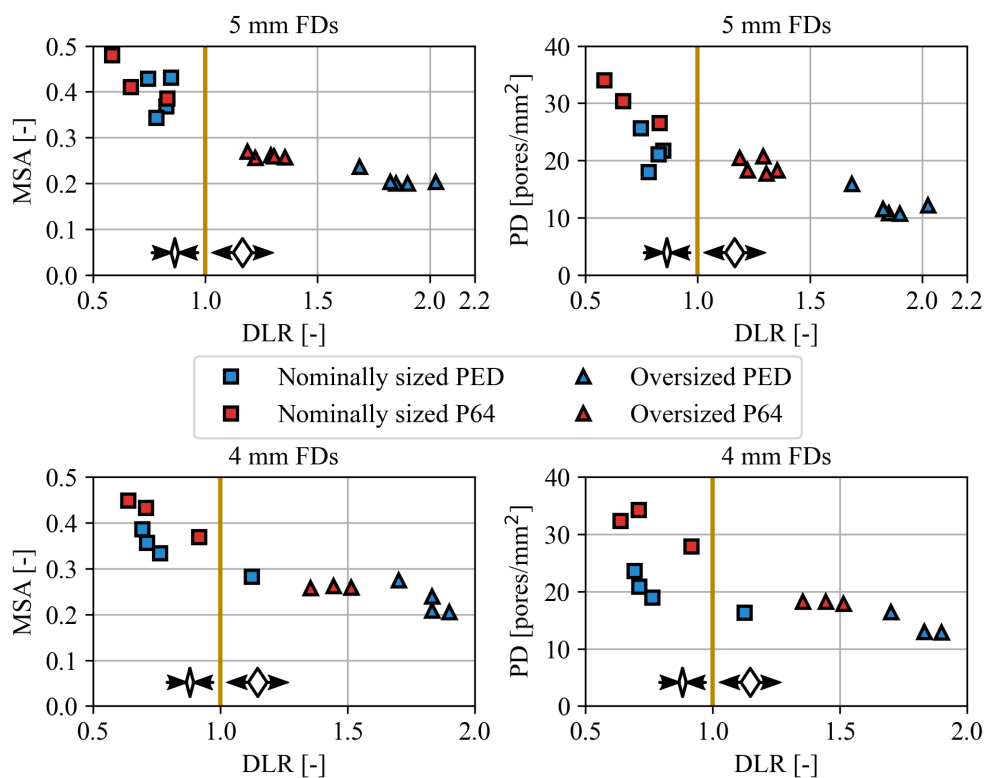


Figure 8: The effects of longitudinal compression or elongation in the cases of FD5 in Tube5 and Tube4 (top row), and FD4 in Tube4 and Tube3 (bottom row) measurements, the metallic surface area (left) and pore density (right) as the function of the deployment length ratio. The vertical yellow lines represent the nominal deployment length, the small pictograms represent the longitudinally compressed and elongated deployment scenarios. Blue markers correspond to PED, while red markers correspond to P64 measurements. Squares are the nominally sized and triangles are the oversized cases.

Based on the results, ANOVA was performed. Significant connections between the HR, MSA, PD and the manufacturer, radial and longitudinal sizing was sought. The ANOVA proved, that the radial and longitudinal sizing both have significant effect on the linear coefficient of the HR curve ($p < 0.0021$ and $p < 0.00133$, respectively), while there is no significant effect of the manufacturers on either coefficient of the HR curve. The manufacturer has significant effect only on the PD values, which is trivial based on the braided geometry.

This section provides quantitative differences between FD deployment scenarios. Based on these data, neurointerventionalists can objectively choose the device before surgery. Furthermore these values can be used in the numerical simulations when the FD is modelled as a porous medium.

Contribution 4

ANOVA was performed based on in-vitro measurements of the Pipeline Embolization Device (Medtronic plc, Minneapolis, MN, USA) and the P64 device (Phenox Inc., Bochum, Germany). The manufacturer has no significant effect on the linear and quadratic coefficients of the pressure drop on the device (hydrodynamic resistance), but radial sizing and longitudinal sizing has significant effect on the linear coefficients ($p < 0.0021$ and $p < 0.00133$, respectively). According to the results, an oversized device (when the nominal diameter of the device is larger than the deployed diameter) produces less hydrodynamic resistance compared to a nominally sized device (when the deployed and nominal diameters are equal). Similarly, an elongated device produces less hydrodynamic resistance compared to a compressed device.

Related publications: [J5] and [J6].

Published papers

Journal articles

- [J1] **D. Gyürki**, T. Horváth, S. Till, A. Egri, C. Celeng, G. Paál, B. Merkely, P. Maurovich-Horvat, and G. Halász, "Central arterial pressure and patient-specific model parameter estimation based on radial pressure measurements", *Computer Methods in Biomechanics and Biomedical Engineering*, vol. 26, no. 11, pp. 1320-1329, 2023. doi: 10.1080/10255842.2022.2115292, IF(2022): 1.6
- [J2] **D. Gyürki**, P. Sótonyi, and G. Paál, "Central arterial pressure estimation based on two peripheral pressure measurements using one-dimensional blood flow simulations", *Computer Methods in Biomechanics and Biomedical Engineering*, vol. 27, no. 6, pp. 689-699, 2024. doi: 10.1080/10255842.2023.2199112, IF(2022): 1.6
- [J3] **D. Gyürki**, and G. Paál, "Investigating Particle Paths in Intracranial Aneurysms: A Parametric Study", *Periodica Polytechnica Mechanical Engineering*, vol. 67, no. 4, pp. 350-360, 2023. doi: 10.3311/PPme.23482
- [J4] G. Závodszy, **D. Gyürki**, G. Károlyi, I. Szikora, and G. Paál, "Fractals and Chaos in the Hemodynamics of Intracranial Aneurysms", *Advances in Neurobiology*, vol. 36, pp. 397-412, 2024. doi:10.1007/978-3-031-47606-8_20
- [J5] B. Csippa, **D. Gyürki**, G. Závodszy, G. Paál, and I. Szikora, "Hydrodynamic Resistance of Intracranial Flow-Diverter Stents: Measurement Description and Data Evaluation", *Cardiovascular Engineering and Technology*, vol. 11, pp. 1-13, 2020. doi: 10.1007/s13239-019-00445-y, IF(2020): 2.495
- [J6] **D. Gyürki**, B. Csippa, G. Paál, and I. Szikora, "Impact of Design and Deployment Technique on the Hydrodynamic Resistance of Flow Diverters", *Clinical Neuroradiology*, vol. 32, pp. 107-115, 2022. doi: 10.1007/s00062-021-01106-1, IF(2021): 3.156

Conference papers

- [C1] **G. Dániel**, and P. György, "Aneurizmában megjelenő kaotikus pályák vizsgálata fraktálokra jellemző mérőszámokkal", *XXIX. Nemzetközi Gépészeti Találkozó OGÉT*, 2021.04.23., Online, (2021)
- [C2] **D. Gyürki**, I. Szikora, and G. Paál, "Calculating Particle Residence Times in Vessel Geometries with Aneurysm", *The 18th International Conference on Fluid Flow Technologies*, 2022.08.30.-2022.09.02., Budapest, (2022)

References

- [1] A. P. Avolio, “Multi-branched model of the human arterial system,” *Medical & Biological Engineering & Computing*, vol. 18, no. 6, pp. 709–718, 1980.
- [2] A. J. Geers, H. G. Morales, I. Larrabide, C. Butakoff, P. Bijlenga, and A. F. Frangi, “Wall shear stress at the initiation site of cerebral aneurysms,” *Biomechanics and Modeling in Mechanobiology*, vol. 16, no. 1, pp. 97–115, 2017.
- [3] K. Sunderland and J. Jiang, “Multivariate analysis of hemodynamic parameters on intracranial aneurysm initiation of the internal carotid artery,” *Medical Engineering and Physics*, vol. 74, no. xxxx, pp. 129–136, 2019.
- [4] J. R. Cebal, F. Mut, J. Weir, and C. M. Putman, “Association of hemodynamic characteristics and cerebral aneurysm rupture,” *American Journal of Neuroradiology*, vol. 32, no. 2, pp. 264–270, 2011.
- [5] P. Berg, C. Roloff, O. Beuing, S. Voss, S. I. Sugiyama, N. Aristokleous, A. S. Anayiotos, N. Ashton, A. Revell, N. W. Bressloff, A. G. Brown, B. J. Chung, J. R. Cebal, G. Copelli, W. Fu, A. Qiao, A. J. Geers, S. Hodis, D. Dragomir-Daescu, E. Nordahl, Y. B. Suzen, M. O. Khan, K. Valen-Sendstad, K. Kono, P. G. Menon, P. G. Albal, O. Mierka, R. Münster, H. G. Morales, O. Bonnefous, J. Osman, L. Goubergrits, J. Pallares, S. Cito, A. Passalacqua, S. Piskin, K. Pekkan, S. Ramalho, N. Marques, S. Sanchi, K. R. Schumacher, J. Sturgeon, H. Švihlová, J. Hron, G. Usera, M. Mendina, J. Xiang, H. Meng, D. A. Steinman, and G. Janiga, “The Computational Fluid Dynamics Rupture Challenge 2013 - Phase II: Variability of Hemodynamic Simulations in Two Intracranial Aneurysms,” *Journal of Biomechanical Engineering*, vol. 137, no. 12, 2015.
- [6] M. H. Babiker, L. F. Gonzalez, J. Ryan, F. Albuquerque, D. Collins, A. Elvikis, and D. H. Frakes, “Influence of stent configuration on cerebral aneurysm fluid dynamics,” *Journal of Biomechanics*, vol. 45, no. 3, pp. 440–447, 2012.
- [7] B. T. Jankowitz, B. A. Gross, S. Seshadhri, G. Girdhar, A. Jadhav, T. G. Jovin, and J. M. Wainwright, “Hemodynamic differences between Pipeline and coil-adjunctive intracranial stents,” *Journal of NeuroInterventional Surgery*, vol. 11, no. 9, pp. 908–911, 2019.
- [8] S. Fukuda, Y. Shimogonya, M. Nakamura, T. Yamada, K. Suzuki, Y. Yamamoto, K. Kanou, N. Okada, F. Pan, T. Okudaira, and S. Kuwahara, “Review on the formation and growth of cerebral aneurysms,” *Journal of Biorheology*, vol. 33, no. 2, pp. 43–52, 2019.

-
- [9] A. Herbert, J. K. Cruickshank, S. Laurent, P. Boutouyrie, K. Shimada, K. Kario, H. Miyashita, K. Eguchi, K. Kohara, Y. Tabara, Y. Imai, S. Ito, J. Hashimoto, K. Uchiba, H. Suzuki, T. Takenaka, K. Takazawa, M. Kino, A. Yamashina, H. Tomiyama, Y. Dohi, H. Takase, X. Jouven, J. P. Empana, B. Pannier, F. Thomas, E. Prescott, J. Janner, C. McEniery, J. Cockcroft, I. Wilkinson, M. J. Roman, R. B. Devereux, V. Teal, R. Townsend, S. Vermeersch, E. R. Rietzschel, L. Van Bortel, M. L. De Buyzere, P. Segers, T. C. Gillebert, J. G. Wang, Y. Li, J. Lazar, L. Saliccioli, P. Cunha, P. Oliveira, J. Cotter, I. Vila, N. Sousa, J. Chirinos, J. Medina-Lezama, T. Weber, M. Rammer, M. F. O'Rourke, E. Bernd, E. Lassnig, M. Porodko, M. Ammer, S. Wassertheurer, A. Adji, S. Rosenkranz, C. Punzengruber, E. Kvas, C. Dufouil, C. Tzourio, G. Nijpels, J. M. Dekker, C. D. Stehouwer, I. Ferreira, J. W. Twisk, Y. M. Smulders, R. J. Van De Laar, C. J. Van Kallen, M. M. Van Greevenbroek, C. G. Schalkwijk, C. Vlachopoulos, C. Aznaouridis, D. Terentes-Printzios, P. Xaplanteris, C. Stefanadis, A. E. Schutte, C. M. Fourie, J. M. Van Rooyen, A. Mahmud, J. Feely, L. Ghiadoni, F. Stea, R. M. Bruno, G. Cartoni, S. Armenia, S. Taddei, J. Seidlerova, J. Vanek, J. Filipovsky, O. Mayer, L. Lind, I. Soveri, B. Fellström, M. Zilmer, M. C. Cavallini, R. Pini, M. Di Bari, N. Marchionni, G. Masotti, G. Schillaci, G. Pucci, F. Battista, L. Settimi, M. A. Crilly, V. Kumar, H. J. Clark, N. W. Scott, A. G. Macdonald, D. J. Williams, G. S. Hillis, A. J. Lee, A. De Vries, G. R. Small, A. Zanchetti, G. Bilo, C. Taurino, J. D. McClure, M. P. Schneider, K. Kawecka-Jaszcz, K. Stolarz-Skrzypek, Ł. Klima, J. A. Staessen, T. Kuznetsova, J. Redon, F. Martinez, E. A. Rosei, O. Melander, F. Zannad, P. Rossignol, C. Collin, L. Lonati, A. F. Dominiczak, O. Petrak, B. Štrauch, J. Rosa, J. Widimský, A. Pipingas, M. P. Pase, N. A. Grima, C. Stough, E. Harris, L. Sellick, H. Macpherson, J. M. Pascualab, E. Rodilla, J. A. Costa, T. Simon, C. Delles, J. A. Dymott, U. Neisius, D. M. Carty, P. Fesler, M. L. Muiesan, M. Salvettia, A. Paini, A. Tisler, Zofi, A. Marton, T. El Haj Othmane, O. Cseprekal, P. Studinger, N. N. I. N. Ibrahim, A. H. G. Rasool, A. R. A. Rahman, A. R. Wong, A. D. Protogerou, T. G. Papaioannou, P. P. Sfikakis, Y. Fu, J. Hu, L. Zhao, N. Li, X. Jiang, E. Ok, M. S. Demirci, O. Gungor, I. A. Orlova, Z. N. Blankova, E. M. Seredenina, F. T. Ageev, I. A. Orlova, I. V. Barinova, E. M. Seredenina, F. T. Ageev, J. Bellien, M. Iacob, C. Thuiliez, Joannides, I. Mintale, G. Latkovskis, M. Berzina, M. Zabunova, A. Krallisa, H. Smulyan, M. Safar, A. Zhadan, V. Tselukyo, T. Bregvadze, A. Aydin, and Y. Von Kodolitsch, "Establishing reference values for central blood pressure and its amplification in a general healthy population and according to cardiovascular risk factors," *European Heart Journal*, vol. 35, no. 44, pp. 3122–3133, 2014.
- [10] C. Vlachopoulos, K. Aznaouridis, M. F. O'Rourke, M. E. Safar, K. Baou, and C. Stefanadis, "Prediction of cardiovascular events and all-cause mortality with central haemodynamics: A systematic review and meta-analysis," *European Heart Journal*, vol. 31, no. 15, pp. 1865–1871, 2010.

-
- [11] T. Papaioannou, A. Protogerou, K. Stamatelopoulos, M. Vavuranakis, and C. Stefanadis, "Non-Invasive Methods and Techniques for Central Blood Pressure Estimation: Procedures, Validation, Reproducibility and Limitations," *Current Pharmaceutical Design*, vol. 15, no. 3, pp. 245–253, 2009.
- [12] G. Bárdossy and G. Halász, "Modeling blood flow in the arterial system," *Periodica Polytechnica Mechanical Engineering*, vol. 55, no. 1, pp. 49–55, 2011.
- [13] G. Bárdossy and G. Halász, "A " backward" calculation method for the estimation of central aortic pressure wave in a 1D arterial model network," *Computers and Fluids*, vol. 73, pp. 134–144, 2013.
- [14] J. J. Wang and K. H. Parker, "Wave propagation in a model of the arterial circulation," *Journal of Biomechanics*, vol. 37, no. 4, pp. 457–470, 2004.
- [15] C. H. Chen, E. Nevo, B. Fetcs, P. H. Pak, F. C. Yin, W. L. Maughan, and D. A. Kass, "Estimation of central aortic pressure waveform by mathematical transformation of radial tonometry pressure data [1] (multiple letters)," *Circulation*, vol. 95, no. 7, pp. 1827–1836, 1997.
- [16] P. W. Longest and C. Kleinstreuer, "Numerical Simulation of Wall Shear Stress Conditions and Platelet Localization in Realistic End-to-Side Arterial Anastomoses," *Journal of Biomechanical Engineering*, vol. 125, no. 5, pp. 671–681, 2003.
- [17] A. Shamloo and M. Forouzandehmehr, "Personalised deposition maps for micro- and nanoparticles targeting an atherosclerotic plaque: attributions to the receptor-mediated adsorption on the inflamed endothelial cells," *Biomechanics and Modeling in Mechanobiology*, vol. 18, no. 3, pp. 813–828, 2019.
- [18] G. Závodszy, G. Károlyi, and G. Paál, "Emerging fractal patterns in a real 3D cerebral aneurysm," *Journal of Theoretical Biology*, vol. 368, pp. 95–101, 2015.
- [19] K. Valen-Sendstad, M. Piccinelli, and D. A. Steinman, "High-resolution computational fluid dynamics detects flow instabilities in the carotid siphon: Implications for aneurysm initiation and rupture?," *Journal of Biomechanics*, vol. 47, no. 12, pp. 3210–3216, 2014.
- [20] J. Latt, O. Malaspinas, D. Kontaxakis, A. Parmigiani, D. Lagrava, F. Brogi, M. B. Belgacem, Y. Thorimbert, S. Leclaire, S. Li, F. Marson, J. Lemus, C. Kotsalos, R. Conrardin, C. Coreixas, R. Petkantchin, F. Raynaud, J. Beny, and B. Chopard, "Palabos: Parallel Lattice Boltzmann Solver," *Computers and Mathematics with Applications*, vol. 81, pp. 334–350, 2021.

-
- [21] Hetts, S.W., A. Turk, J. D. English, C. F. Dowd, J. Mocco, C. Prestigiacomo, G. Nesbit, S. G. Ge, J. N. Jin, K. Carroll, Y. Murayama, A. Gholkar, S. Barnwell, D. Lopes, and S. C. Johnston, “Stent-assisted coiling versus coiling alone in unruptured intracranial aneurysms in the matrix and platinum science trial: Safety, efficacy, and mid-term outcomes,” *American Journal of Neuroradiology*, vol. 35, no. 4, pp. 698–705, 2014.
- [22] T. Becske, W. Brinjikji, M. B. Potts, D. F. Kallmes, M. Shapiro, C. J. Moran, E. I. Levy, C. G. McDougall, I. Szikora, G. Lanzino, H. H. Woo, D. K. Lopes, A. H. Siddiqui, F. C. Albuquerque, D. J. Fiorella, I. Saatci, S. H. Cekirge, A. L. Berez, D. J. Cher, Z. Berentei, M. Marosfoi, and P. K. Nelson, “Long-Term clinical and angiographic outcomes following pipeline embolization device treatment of complex internal carotid artery aneurysms: Five-year results of the pipeline for uncoilable or failed aneurysms trial,” *Neurosurgery*, vol. 80, no. 1, pp. 40–48, 2017.
- [23] M. Shapiro, E. Raz, T. Becske, and P. K. Nelson, “Variable porosity of the pipeline embolization device in straight and curved vessels: A guide for optimal deployment strategy,” *American Journal of Neuroradiology*, vol. 35, no. 4, pp. 727–733, 2014.
- [24] M. J. Kole, T. R. Miller, G. Cannarsa, A. Wessell, S. Jones, E. Le, G. Jindal, F. Aldrich, J. M. Simard, and D. Gandhi, “Pipeline embolization device diameter is an important factor determining the efficacy of flow diversion treatment of small intracranial saccular aneurysms,” *Journal of NeuroInterventional Surgery*, vol. 11, no. 10, pp. 1004–1008, 2019.
- [25] Y. Zhang, W. Chong, and Y. Qian, “Investigation of intracranial aneurysm hemodynamics following flow diverter stent treatment,” *Medical Engineering and Physics*, vol. 35, no. 5, pp. 608–615, 2013.
- [26] Á. Ugron, I. Szikora, and G. Paál, “Measurement of flow diverter hydraulic resistance to model flow modification in and around intracranial aneurysms,” *Interventional Medicine and Applied Science*, vol. 6, no. 2, pp. 61–68, 2014.